

Temperature Dependence of Optical Gain and Loss in $\lambda \approx 8.2\text{--}10.2 \mu\text{m}$ Quantum-Cascade Lasers

Zhijun Liu, Claire F. Gmachl, *Senior Member, IEEE*, Liwei Cheng, Fow-Sen Choa, *Senior Member, IEEE*, Fred J. Towner, Xiaojun Wang, and Jenyu Fan

Abstract—Temperature-dependent optical gain and waveguide loss have been measured for continuous-wave operated quantum-cascade lasers with wavelengths between 8.2 and 10.2 μm up to room temperature using the Hakki–Paoli method. The gain coefficient decreases with increasing temperature, and is close to the designed value for vertical transition lasers, but smaller than the designed value for diagonal transition lasers. The waveguide loss, however, is two to three times higher than calculated from free carrier absorption, and can be nearly constant, increase or decrease with temperature depending on sample design, which indicates that it is dominated by another mechanism other than plain free carrier absorption. One likely factor resulting in high waveguide loss is intersubband resonant absorption into higher lying states.

Index Terms—Midinfrared, optical gain, quantum-cascade (QC) laser, waveguide loss.

I. INTRODUCTION

QUANTUM-CASCADE (QC) lasers are an emerging midinfrared semiconductor light source which attract considerable interest for midinfrared sensor systems, especially for high sensitivity and selectivity detection of chemical vapors in security, medical, and environmental applications [1]–[4]. Owing to improved laser design, material growth and device packaging, the performance of QC lasers has improved significantly, and high-power room-temperature continuous-wave (CW) operation has been demonstrated repeatedly for wavelengths between 3.8 and 10.6 μm [5]–[10]. Optical gain and waveguide loss are two important parameters in the understanding of QC laser performance and in improving laser designs to achieve even better performance. However, high-quality data regarding these two parameters are very limited in the current literature for high performance QC lasers, with the waveguide loss being reported only at room temperature in some cases [5], [8], [9]. Here, by using the Hakki–Paoli method [11], which we found to be the most

reliable, we performed a systematic study of the optical gain and waveguide loss versus temperature for room temperature CW QC lasers designed with vertical or diagonal transitions at various wavelengths between 8.2 and 10.2 μm . We have measured QC lasers with the same waveguide but different active region designs, and QC lasers that are fabricated as ridge waveguides or buried heterostructure lasers. Besides confirming the expected magnitude and temperature dependence of the gain coefficient, our results indicate a two to three times higher waveguide loss than calculated from free carrier absorption. Also, the waveguide loss can be nearly constant, increase or decrease with temperature depending on the laser design, which suggests a dominant loss mechanism other than free carrier absorption.

II. EXPERIMENT

There are two straightforward methods for measuring the optical gain and waveguide loss in QC lasers: the “1/L” method and the Hakki–Paoli method [12], [13]. The “1/L” method relies on measuring threshold of several reliable devices of different cavity lengths. The second method, the Hakki–Paoli method, utilizes the subthreshold amplified spontaneous emission spectra of a single device. We used both methods in our initial experiments testing a 10.2- μm QC laser design. The results from both methods agree well at room temperature, but do not agree at cryogenic temperatures. The reason is that for the “1/L” method, the gain coefficient and waveguide loss are very sensitive to the accuracy of threshold current measurement. At low temperature, because the laser thresholds are small values, the uncertainties in threshold due to performance variation from device to device result in a large change in waveguide loss and gain coefficient. Conversely, the Hakki–Paoli method relies on measurements of a single device, which circumvents the difficulty of inter-device fluctuations and thus has been employed in the following experiments.

The samples studied in this work are listed in Table I. QCV1, QCV2, QCV3 are 8.2, 9.6, and 10.2 μm “vertical-transition” QC lasers, respectively. They are based on a two phonon resonance design [14] which is widely employed in current high performance QC lasers. QCD1 and QCD2 are diagonal transition lasers at $\lambda \sim 9.8$ and 10.1 μm , respectively. Their laser transitions were designed as diagonal transitions with a two phonon resonance scheme for carrier depopulation. For each sample, a 1.5-mm-long laser is operated in CW and its subthreshold amplified spontaneous emission spectrum is recorded with a Magna 860 Fourier transform infrared spectrometer (FTIR) and cooled MCT detector averaging 200 scans at 0.125 cm^{-1} resolution. The spectra of each sample are measured at different

Manuscript received July 6, 2007; revised November 27, 2007. This work was supported in part by DARPA L-PAS, DARPA-EMIL and MIRTHER (NSF-ERC).

Z. Liu and C. F. Gmachl are with the Department of Electrical Engineering and the Princeton Institute for the Science and Technology of Materials, Princeton University, Princeton, NJ 08544 USA (e-mail: zhijunl@princeton.edu; cgmachl@princeton.edu).

L. Cheng and F.-S. Choa are with the Department of Computer Science and Electrical Engineering, University of Maryland, Baltimore, MD 21250 USA (e-mail: cheng3@umbc.edu; choa@umbc.edu).

F. J. Towner is with Maxion Technologies Inc., Hyattsville, MD 20782 USA (e-mail: ftowner@maxion.com).

X. Wang and J. Fan are with AdTech Optics, City of Industry, CA 91748 USA (e-mail: xiaojun.wang@atoptics.com; jenyu.fan@atoptics.com).

Digital Object Identifier 10.1109/JQE.2008.917273

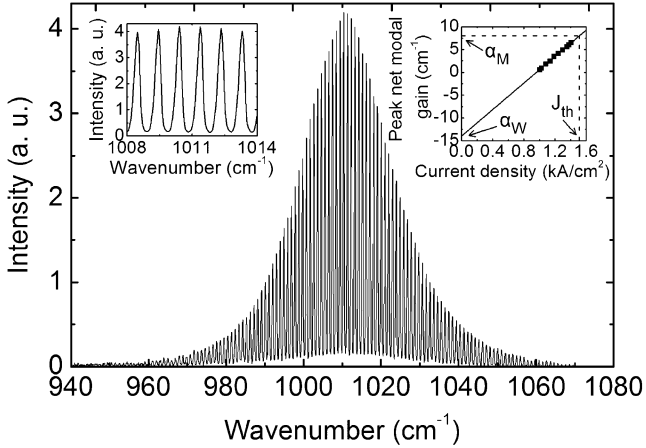


Fig. 1. Typical subthreshold amplified spontaneous emission spectrum of a 1.5-mm-long 16- μm -wide, CW operated QC laser at $\lambda \sim 10.2 \mu\text{m}$ (QCV3). The laser is operated at 0.33-A current at 120-K heat sink temperature. The left inset shows the central Fabry-Perot modes in greater detail. The right inset shows peak net modal gain as a function of the injection current density, where the linear least squares fit (solid line) gives the gain coefficient and waveguide loss from its slope and y axis intercept, respectively.

TABLE I
QC LASER SAMPLES

Sample label	Laser design	Wavelength (μm)	Fabrication
QCV1	Vertical	8.2	Ridge waveguide
QCV2	Vertical	9.6	Ridge waveguide
QCV3	Vertical	10.2	Ridge waveguide; Buried heterostructure
QCD1	Diagonal	9.8	Ridge waveguide
QCD2	Diagonal	10.1	Ridge waveguide

heat sink temperatures up to the maximum CW operating temperature. A typical spectrum for the 10.2- μm vertical transition QC laser (QCV3) is shown in Fig. 1. The left inset shows the Fabry-Perot modes at the central part of the spectrum in greater detail. The spectrum oscillates periodically without any additional maxima and minima, indicating single lateral mode emission as required by the Hakki-Paoli method.

The peak modal net gain can be calculated from the Fabry-Perot fringe contrast using

$$g\Gamma J - \alpha_W = -\frac{1}{L} \left[\ln \left(\frac{\sqrt{P_{\max}/P_{\min}} + 1}{\sqrt{P_{\max}/P_{\min}} - 1} \right) - \ln \left(\frac{1}{R} \right) \right] \quad (1)$$

where g is the gain coefficient, Γ is the optical mode confinement factor, J is the injection current density, L is the cavity length, and R is the facet reflectivity. P_{\max} and P_{\min} are the neighboring maxima and minima of the spectral intensity. By calculating the net modal gain from the spectra at different injection currents (right inset in Fig. 1), the linear fit gives the information of gain coefficient and waveguide loss from its slope and y axis intercept, respectively. As an example, the right inset

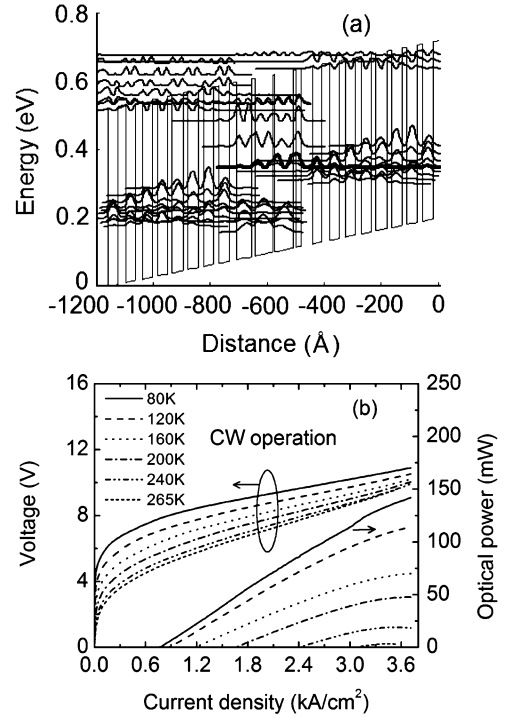


Fig. 2. (a) Conduction band diagram of a portion of the active regions and injectors and the moduli squared of the relevant wave functions of sample QCV3 under a bias of 4 V. The bold curve represents the upper laser level. (b) CW light-current-voltage curves of a 3.5-mm-long 17.7- μm -wide QC laser at $\lambda \sim 10.2 \mu\text{m}$ (QCV3) at different heat sink temperatures.

in Fig. 1 shows the peak net modal gain as a function of current density for QCV3 at heat sink temperature of 120 K, and its linear least squares fit gives a gain coefficient of 14.55 cm/kA and waveguide loss of 14 cm^{-1} . During this procedure, we extrapolated the net gain to zero current, which is supported by the energy band diagram and current-voltage curves shown in Fig. 2. At a voltage of 4 V where current starts flowing for the 120 K data, the energy band diagram in Fig. 2(a) shows no pathways of carrier leakage as the ground state of one injector is already well separated from the lower states of the following active region. For voltage higher than 4 V, the injector aligns fully with the upper laser level, and the current is carried by electron tunneling from the injector ground state into the upper laser level. Therefore, we consider it valid to extrapolate the net gain to zero current to extract the gain coefficient and waveguide loss.

III. RESULTS AND DISCUSSION

The laser structure of sample QCV1 and its device performance have been described in [10]. A 3.5-mm-long 8- μm -wide, deep-etched ridge waveguide laser functions in CW mode above room temperature. The measured gain coefficient and waveguide loss from a 1.5-mm-long 9- μm -wide device are shown in Fig. 3. The device is operated in CW mode. The bottom x axis of Fig. 3 refers to the laser active core temperature, which is obtained by evaluating the temperature difference between laser core and heat sink from the pulsed and CW threshold current

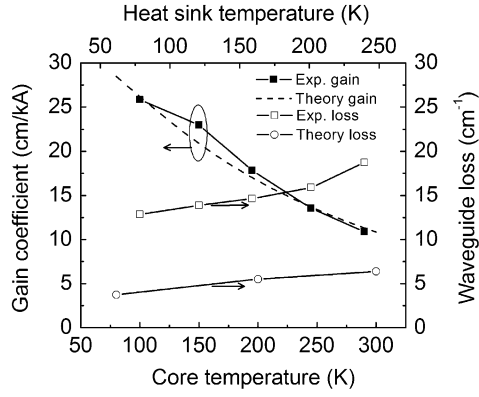


Fig. 3. Gain coefficient (solid squares) and waveguide loss (open squares) versus core temperature for a 1.5-mm-long 9- μm -wide ridge waveguide QC laser at $\lambda\sim 8.2\ \mu\text{m}$ (QCV1). The dashed line is the theoretical gain coefficient, and the circles are calculated free carrier absorption from the design. Lines through data points are guides to the eye.

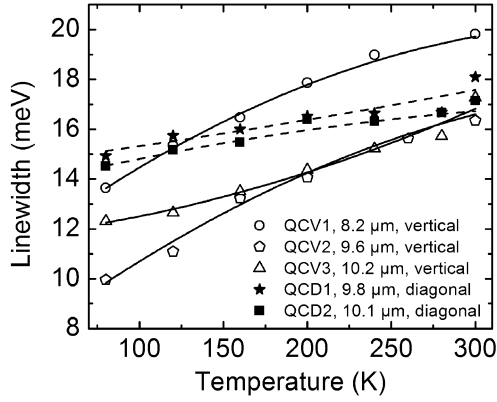


Fig. 4. FWHM linewidth of the electroluminescence of the laser transition at different heat sink temperatures for all samples studied in this work. Solid and dashed lines are second order polynomial fit to the data points. Data are obtained in pulsed mode under injection currents close to the laser threshold.

densities of the device. The gain coefficient decreases as temperature increases, and agrees well with the theoretical values, which are calculated as [15]

$$g\Gamma = \tau_3 \left(1 - \frac{\tau_2}{\tau_{32}}\right) \frac{4\pi e z^2 \Gamma}{\lambda_0 \varepsilon_0 n_{\text{eff}} L_p (2\gamma)} \quad (2a)$$

$$\tau_i(T) = \tau_{i0} \frac{1}{1 + \frac{2}{\exp\left(\frac{E_{LO}}{kT}\right) - 1}} \quad (2b)$$

where λ_0 is the laser wavelength in vacuum, ε_0 is vacuum dielectric constant, n_{eff} is the effective refractive index of the mode, L_p is the length of one period of the active region, z is the dipole matrix element, 2γ is the full-width at half-maximum (FWHM) value of the luminescence spectrum determined by experiment, as given in Fig. 4. τ_3 and τ_2 are the lifetimes for the upper and lower laser levels, respectively, τ_{32} is the non-radiative transition lifetime between upper and lower laser levels, τ_{i0} is the low temperature lifetime, E_{LO} is the energy of longitudinal optical phonon, k is the Boltzman constant, and T is the temperature.

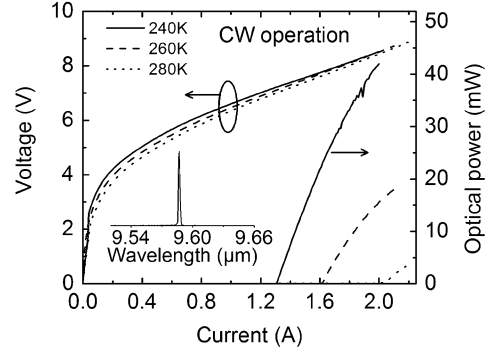


Fig. 5. CW light-current-voltage curves for a 3.5-mm-long 17- μm -wide, back-facet HR coated QC laser at $\lambda\sim 9.6\ \mu\text{m}$ (QCV2). The inset shows a laser spectrum at 240 K and 1.38 A.

The waveguide loss of device QCV1 increases from 13 to 18 cm^{-1} as the temperature increases from 100 to 300 K, and is more than two times of the calculated free carrier absorption. Here the free carrier absorption is calculated based on Drude model, and an increase in the free carrier absorption with temperature is due to the decrease in electron mobility [16], [17]. The electron scattering lifetime for InP cladding layer is taken as 0.37, 0.18, and 0.15 ps at 80, 200, and 300 K, respectively, which are obtained from the electron mobility data in [17]. For the active core region, the electron scattering lifetime is 0.1, 0.074, and 0.066 ps at 80, 200, 300 K, respectively, which are extracted from the measured electroluminescence linewidth in Fig. 4 by assuming a homogeneous broadening due to interface scattering. The designed doping levels of 1×10^{17} and $8 \times 10^{18}\ \text{cm}^{-3}$ are used for the InP cladding layer and plasmon layer, and the designed average doping level $3.25 \times 10^{16}\ \text{cm}^{-3}$ is used for the active core in the calculation. These carrier concentrations are assumed to be independent of temperature as indicated in [16]. This same procedure is applied for the other four samples except that the actual measured carrier concentrations are used for samples QCV3 and QCD2, which are two times higher than their designed doping levels.

Next, we discuss a second vertical transition sample QCV2, which is designed as a two phonon resonance at $\lambda\sim 9.6\ \mu\text{m}$. The performance of a 3.5-mm-long 17- μm -wide, ridge waveguide, high reflectivity (HR) back facet coated QC laser is shown in Fig. 5. It functions in CW up to 280 K with an optical power of 3.6 mW. The gain coefficient and waveguide loss measured from a 1.5-mm-long 16- μm -wide, ridge waveguide laser is given in Fig. 6. Again, the gain coefficient agrees well with the design. The waveguide loss is more than two times of the calculated free carrier absorption, and is almost a constant with temperature around $12\ \text{cm}^{-1}$.

We further measured a third sample, QCV3, which is a 10.2 μm QC laser based on a two phonon resonance with a vertical optical transition. This sample is processed into both ridge waveguide and buried heterostructure (BH) lasers with lateral InP regrowth. The device performance is shown in Fig. 7. A 3.5-mm-long 15.6- μm -wide, ridge waveguide laser operates in CW up to 257 K. The InP lateral regrowth and HR back facet coating give 25 and 19 K improvements in maximum CW operation temperature, respectively, and a 3.5-mm-long 15.4- μm -wide HR back facet coated, buried

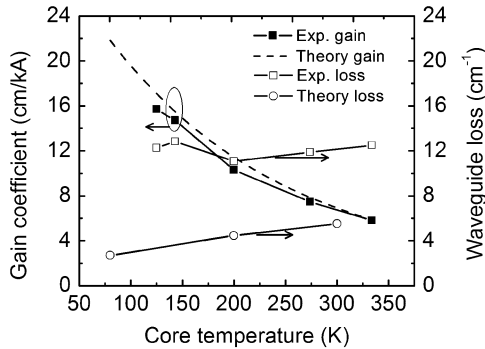


Fig. 6. Gain coefficient (solid squares) and waveguide loss (open squares) versus core temperature for a 1.5-mm-long 16- μm -wide ridge waveguide QC laser at $\lambda \sim 9.6 \mu\text{m}$ (QCV2). The dashed line is the theoretical gain coefficient, and the circles are calculated free carrier absorption from the design. Lines through data points are guides to the eye.

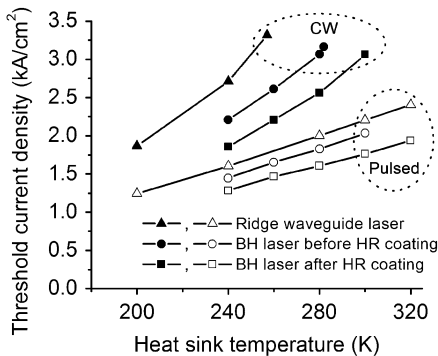


Fig. 7. Pulsed and CW threshold current densities versus heat sink temperature of a 3.5-mm-long, 15.6- μm -wide, ridge waveguide QC laser at $\lambda \sim 10.2 \mu\text{m}$, and of a 3.5-mm-long 15.4- μm -wide, BH QC laser from the same wafer (QCV3) before and after HR coating on the back facet.

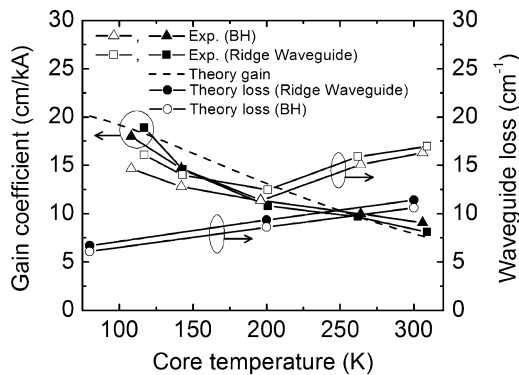


Fig. 8. Gain coefficient and waveguide loss versus core temperature for a 1.5-mm-long 16- μm -wide, ridge waveguide QC laser (squares) and a buried heterostructure QC laser (triangles) at $\lambda \sim 10.2 \mu\text{m}$ (QCV3). The dashed line is the theoretical gain coefficient, and the solid and open circles are calculated free carrier absorption for the ridge waveguide and buried heterostructure lasers, respectively. Lines through data points are guides to the eye.

heterostructure device functions in CW at room temperature. The gain coefficients and waveguide losses for 1.5-mm-long 16- μm -wide ridge waveguide and buried heterostructure lasers are given in Fig. 8. It can be seen that the gain coefficients for both lasers are close, and agree well with the designed values. For the waveguide loss, it is again much higher than the calculated free carrier absorption. Also, the buried heterostructure

laser has a slightly lower waveguide loss by $\sim 1 \text{ cm}^{-1}$ than the ridge waveguide laser, which suggests that the side wall $\text{Si}_x\text{N}_y\text{-Ti-Au}$ is not a major loss source for the ridge waveguide structure at these ridge widths. In the calculation of the free carrier absorption for this sample, we used the actual measured doping level from secondary ion mass spectrometry (SIMS) and capacitance-voltage measurements. A prime candidate for the higher than free carrier loss is intersubband resonant absorption, which was found in the energy band diagram (solid arrow) shown in Fig. 9(a). The resonant absorption coefficient can be calculated by using [18]

$$\alpha = n_i g_{i,j}, \quad (3)$$

Here n_i is the carrier concentration on the lower state i , and $g_{i,j}$ is the absorption cross section

$$g_{i,j} = \frac{4\pi e^2 z_{ij}^2 \Gamma}{\epsilon_0 n_{\text{eff}} L_p \lambda_{ij} (2\gamma_{ij})} \left[\frac{\gamma_{ij}^2}{(\hbar\omega - E_{i,j})^2 + \gamma_{ij}^2} \right] \quad (4)$$

where $\hbar\omega$ is the laser photon energy, $E_{i,j}$ is the energy separation between resonant states i and j , λ_{ij} is the corresponding wavelength, and $2\gamma_{ij}$ is the FWHM emission linewidth for transition between them. For the resonant absorption in Fig. 9(a), the thermally populated carrier concentration on the resonant absorption state i takes the form of

$$n_i = n_0 \exp\left(-\frac{\Delta E}{kT}\right) \quad (5)$$

where the n_0 is the doping sheet density, and ΔE is the energy separation between the resonant level i and the injector ground state. The transition linewidth $2\gamma_{ij}$ between these higher lying levels is unknown, and here we used the measured linewidth of the lower lying laser transition as shown in Fig. 4 as a lower bound. The increasing linewidth with temperature is likely due to thermally enhanced interface roughness scattering or non-parabolicity effects. The corresponding absorption is calculated in Fig. 9(b). As temperature increases, the electrons start to populate the state right above the upper laser level, and resonant absorption occurs. Its absorption coefficient increases to 4.5 cm^{-1} at 300 K. This almost accounts for the difference between the measured waveguide loss and calculated free carrier absorption at room temperature. However, there is still a large difference at low temperatures, which needs further study.

Besides the vertical transition QC lasers, we also studied two QC lasers designed as diagonal transition at $\lambda \sim 9.8$ and $10.1 \mu\text{m}$. The electron energy diagram of 9.8- μm QC lasers is shown in Fig. 10. The diagonal laser transition is indicated by the dotted arrow. A two-phonon resonance scheme is used for carrier depopulation. These two samples were processed into ridge waveguide lasers, and the typical device performances are shown in Fig. 11. The 9.8- and 10.1- μm QC lasers function in CW up to 200 and 238 K, respectively. The gain coefficients and waveguide losses for these two samples are shown in Fig. 12. It is seen that the waveguide losses for both samples slightly decrease with temperature and are again much higher than the calculated free carrier absorption. Resonant absorption is a possible factor resulting in this decreasing waveguide loss with temperature. We find a resonant absorption from the

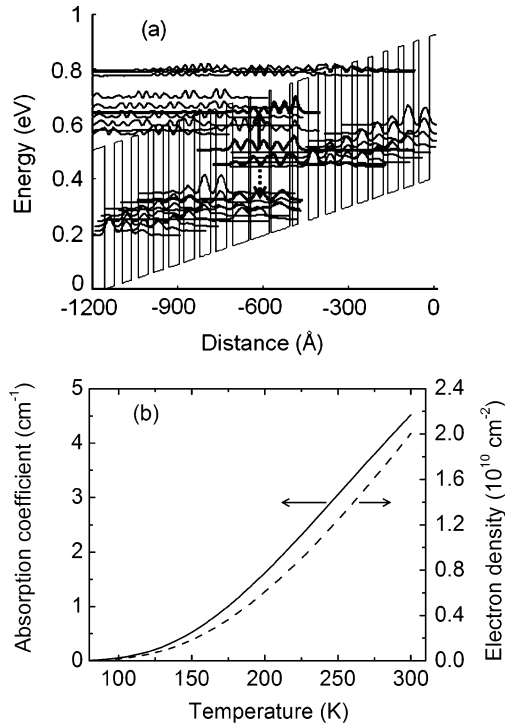


Fig. 9. (a) Conduction band diagram of a portion of the active regions and injectors and the moduli squared of the relevant wave functions of a $\sim 10.2 \mu\text{m}$ QC laser (QCV3) with a 4 quantum well active region. An electric field of 39 kV/cm is applied. The dotted arrow indicates the laser transition. The solid arrow represents a pathway of resonant absorption. (b) Calculated absorption coefficient of the intersubband resonant transition indicated by solid arrow in (a) and thermally excited electron density on the state right above the upper laser level.

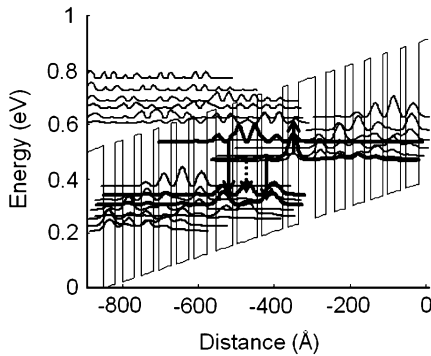


Fig. 10. Conduction band diagram of a portion of the active regions and injectors and the moduli squared of the relevant wave functions of a $\sim 9.8 \mu\text{m}$ diagonal transition QC lasers (QCD1). An electric field of 45 kV/cm is applied. The dotted arrow indicates the laser transition. The solid down arrows represent parasitic optical transitions, and the solid up arrow indicates a pathway of resonant absorption.

injector ground state to a higher excited state for both samples as shown by the solid up arrow in Fig. 10. By assuming the carrier concentration on the injector ground level to be the doping level, the calculated resonant absorption coefficient for QCD2 is shown in Fig. 13. It decreases from 5 to 3.6 cm^{-1} as temperature increases because of a decreasing absorption cross section [see (4)] resulting from the transition linewidth broadening. The gain coefficients follow the trend of the calculated values, but are smaller than what were calculated. One

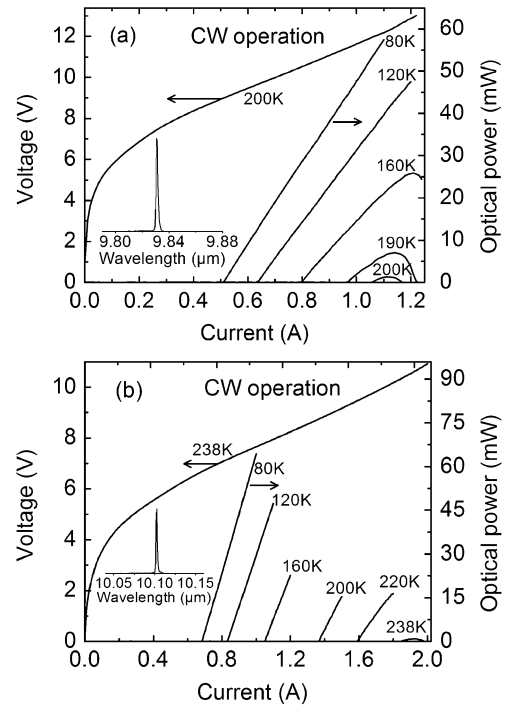


Fig. 11. CW light-current-voltage curves for (a) 3.5-mm-long 10- μm -wide, diagonal transition QC laser at $\lambda \sim 9.8 \mu\text{m}$ (QCD1) and (b) a 3.5-mm-long 16- μm -wide, diagonal transition QC laser at $\lambda \sim 10.1 \mu\text{m}$ (QCD2). The insets show the laser spectra at 80 K and 0.7 A for (a) and 0.72 A for (b).

factor we attribute in part the smaller gain coefficients to is carrier leakage to other transitions, which can be seen from the electroluminescence signals shown in Fig. 14(b). There are two strong parasitic optical transitions for both QCD1 and QCD2. The two parasitic transitions for QCD1 are indicated by solid down arrows in Fig. 10. The peak at $\sim 1195 \text{ cm}^{-1}$ is from the transition between upper laser level and a level beneath the lower laser level, which doesn't affect the gain coefficient. However, The second peak at $\sim 1511 \text{ cm}^{-1}$, which is present only at high temperature ($> 160 \text{ K}$), results from the transition between a higher state above the upper laser level and the lower laser level indicating an electron leakage path. A similar analysis applies to the 10.1- μm diagonal transition QC laser (QCD2). As a comparison with the vertical transition lasers, similar parasitic transitions also exist for the three vertical transition QC lasers, but their intensities are much weaker with less effect on the gain. As an example, the electroluminescence spectrum of sample QCV2 is given in Fig. 14(a). These electroluminescence signals indicate some carrier populations on the upper laser level and higher lying levels for $\text{In}_{0.53}\text{Ga}_{0.47}\text{As}-\text{Al}_{0.48}\text{In}_{0.52}\text{As}$ QC lasers. The electron distribution in $\text{In}_{0.53}\text{Ga}_{0.47}\text{As}-\text{AlAs}_{0.56}\text{Sb}_{0.44}$ QC lasers was studied by Vitiello *et al.* using interband photoluminescence technique [19]. They found that electrons are mainly populated on the injector ground state or the first level in the active region, and the population at upper laser level is negligible. Here the small amounts of electrons on the higher levels in the active region are resolvable from intersubband electroluminescence. From the electroluminescence intensity shown in Fig. 14, the ratio of electrons on the upper laser level to those on the level

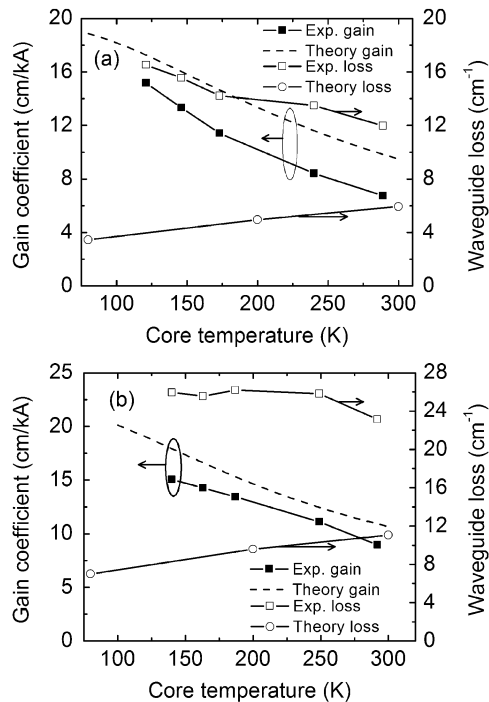


Fig. 12. Gain coefficient (solid squares) and waveguide loss (open squares) versus core temperature for: (a) a 1.5-mm-long 12- μm -wide ridge waveguide diagonal transition QC laser at $\lambda \sim 9.8 \mu\text{m}$ (QCD1); (b) a 1.5-mm-long 15- μm -wide ridge waveguide diagonal transition QC laser at $\lambda \sim 10.1 \mu\text{m}$ (QCD2). The dashed line is the theoretical gain coefficient. The circles show the calculated free carrier absorption (As designed doping levels are used for QCD1, and measured doping levels are used for QCD2). Lines through data points are guides to the eye.

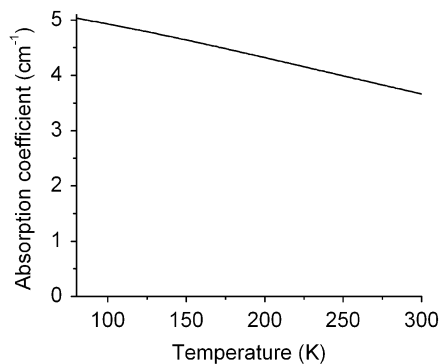


Fig. 13. Calculated absorption coefficient of an intersubband resonant transition from injector ground state to a higher lying level for sample QCD2, which is similar to the resonant absorption indicated by the solid up arrow in Fig. 10.

right above the upper laser level is $\sim 30:1$ for both typical vertical transition laser QCV2 and diagonal transition laser QCD2. From this electron distribution and using a rate equation model including electron injection into both the upper laser level and the level right above, an injection efficiency into upper laser level is deduced as 90% and 82% for QCV2 and QCD2 at room temperature, respectively.

The measured FWHM of the electroluminescence (EL) signal for all samples studied in this work is given in Fig. 4, which has been used in the calculation of gain coefficient. The electroluminescence signal is measured from half circular mesa at different temperatures in pulsed mode under injection currents

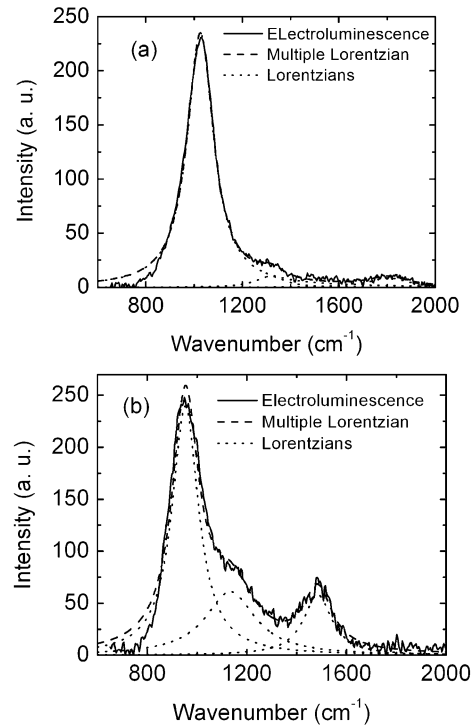


Fig. 14. Room temperature electroluminescence for (a) 9.6- μm vertical transition QC laser (QCV2) and (b) 10.1- μm diagonal transition QC laser (QCD2).

close to the laser threshold. As seen in Fig. 4, by comparing the 8.2- μm vertical transition laser with longer wavelength 9.6- and 10.2- μm vertical transition lasers, the longer wavelength lasers have smaller linewidth. In addition, by comparing the 9.8- and 10.1- μm diagonal transition lasers with the 9.6- and 10.2- μm vertical transition lasers, it is straightforward to see that the diagonal transition lasers have a larger, but less temperature-sensitive linewidth.

Finally, it is interesting to compare samples QCV2, QCV3, and QCD1, since these three samples use the exact same waveguide design, but different active regions. From Figs. 6, 8, and 12(a), different temperature dependences of the waveguide loss are observed. In particular, the waveguide loss remains nearly constant for the 9.6- μm vertical transition laser (Fig. 6), decreases first and then increases for the 10.2- μm vertical transition laser (Fig. 8), and decreases monotonously with temperature for the 9.8- μm diagonal transition laser [Fig. 12(a)]. These complex temperature dependences, which are different from that for free carrier absorption, suggest other loss mechanisms inside the laser active cores. Resonant absorption is a likely factor resulting in this complex temperature-dependence of the waveguide loss. As temperature increases, those absorption levels are shifted either closer to or farther away from resonance. Meanwhile, the transition linewidth broadens. These two effects cause the absorption cross section (4) to either decrease or increase with temperature. This complex behavior together with carrier population through thermal excitation, tunneling and scattering processes can result in both as increasing or decreasing waveguide loss with temperature. Due to uncertainties of some parameters such as transition linewidth, electron energy levels shifts due to temperature or

layer thickness deviation from design, our estimated resonant absorptions can not fully explain the high waveguide loss and different temperature dependence of these samples. So there might be other resonant absorptions which do not show up in our band structure calculation or some additional loss origins such as roughness scattering, defect states, etc., which require further investigations.

IV. SUMMARY

Using the Hakki–Paoli method, we have measured the optical gain and waveguide loss of high temperature CW QC lasers with wavelengths between 8.2 and 10.2 μm at different temperatures. These lasers were designed as vertical or diagonal optical transitions. The results confirm that the gain coefficient decreases with increasing temperature. It is close to the designed value for vertical transition lasers, but smaller than the design for diagonal transition lasers. The measured waveguide loss (12–25 cm^{-1}) is much higher than the calculated free carrier absorption (3–12 cm^{-1}). Intersubband resonant absorption was shown to be an important factor. Also, different temperature dependences of waveguide loss were measured for samples with the same waveguide but different active regions, again confirming the presence of loss mechanisms other than free carrier absorption inside the laser active core.

ACKNOWLEDGMENT

The authors acknowledge the assistance of B. T. Haslam, G. Silva, and J. J. Paulose in early parts of the work.

REFERENCES

- [1] A. A. Kosterev and F. K. Tittel, “Chemical sensors based on quantum cascade lasers,” *IEEE J. Quantum Electron.*, vol. 38, no. 6, pp. 582–591, Jun. 2002.
- [2] R. Jiménez, M. Taslavkov, V. Simeonov, B. Calpini, F. Jeanneret, D. Hofstetter, M. Beck, J. Faist, and H. Van Den Bergh, “Ozone detection by differential absorption spectroscopy at ambient pressure with a 9.6 μm pulsed quantum-cascade laser,” *Appl. Phys. B*, vol. 78, pp. 249–256, 2004.
- [3] M. Pushkarsky, A. Tsekoun, I. G. Dunayevskiy, R. Go, and C. K. N. Patel, “Sub-parts-per-billion level detection of NO_2 using room-temperature quantum cascade lasers,” *Proc. Nat. Acad. Sci. USA*, vol. 103, pp. 10846–10849, 2006.
- [4] M. B. Filho, M. G. da Silva, M. S. Sthel, D. U. Schramm, H. Vargas, A. Miklós, and P. Hess, “Ammonia detection by using quantum-cascade laser photoacoustic spectroscopy,” *Appl. Opt.*, vol. 45, pp. 4966–4971, 2006.
- [5] M. Beck, D. Hofstetter, T. Aellen, J. Faist, U. Oesterle, M. Ilegems, E. Gini, and H. Melchior, “Continuous wave operation of a mid-infrared semiconductor laser at room temperature,” *Science*, vol. 295, pp. 301–305, 2002.
- [6] J. S. Yu, A. Evans, S. Slivken, S. R. Darvish, and M. Razeghi, “Temperature dependent characteristics of $\lambda \sim 3.8 \mu\text{m}$ room-temperature continuous-wave quantum-cascade lasers,” *Appl. Phys. Lett.*, vol. 88, pp. 251118-1–251118-3, 2006.
- [7] S. Slivken, A. Evans, W. Zhang, and M. Razeghi, “High-power, continuous-operation intersubband laser for wavelengths greater than 10 μm ,” *Appl. Phys. Lett.*, vol. 90, pp. 151115-1–151115-3, 2007.
- [8] M. Troccoli, S. Corzine, D. Bour, J. Zhu, O. Assayag, L. Diehl, B. G. Lee, G. Hofler, and F. Capasso, “Room temperature continuous-wave operation of quantum-cascade lasers grown by metal organic vapor phase epitaxy,” *Electron. Lett.*, vol. 41, pp. 1059–1060, 2005.

- [9] L. Diehl, D. Bour, S. Corzine, J. Zhu, G. Hófler, M. Lonéar, M. Troccoli, and F. Capasso, “High-power quantum cascade lasers grown by low-pressure metal organic vapor-phase epitaxy operating in continuous wave above 400 K,” *Appl. Phys. Lett.*, vol. 88, pp. 201115-1–201115-3, 2006.
- [10] Z. Liu, D. Wasserman, S. S. Howard, A. J. Hoffman, C. F. Gmachl, X. Wang, T. Tanbun-Ek, L. Cheng, and F. Choa, “Room-temperature continuous-wave quantum cascade lasers grown by MOCVD without lateral regrowth,” *IEEE Photon. Technol. Lett.*, vol. 18, no. 12, pp. 1347–1349, Jun. 2006.
- [11] B. W. Hakki and T. L. Paoli, “Gain spectra in GaAs double-heterostructure injection lasers,” *J. Appl. Phys.*, vol. 46, pp. 1299–1306, 1975.
- [12] T. Gresch, M. Giovannini, N. Hoyler, and J. Faist, “Quantum cascade lasers with large optical waveguides,” *IEEE Photon. Technol. Lett.*, vol. 18, no. 3, pp. 544–546, Feb. 2006.
- [13] C. Gmachl, H. Y. Hwang, R. Paiella, D. L. Sivco, J. N. Baillargeon, F. Capasso, and A. Y. Cho, “Quantum cascade lasers with low-loss chalcogenide lateral waveguides,” *IEEE Photon. Technol. Lett.*, vol. 13, no. 3, pp. 182–184, Mar. 2001.
- [14] D. Hofstetter, M. Beck, T. Aellen, J. Faist, U. Oesterle, M. Ilegems, E. Gini, and H. Melchior, “Continuous wave operation of a 9.3 μm quantum cascade laser on a Peltier cooler,” *Appl. Phys. Lett.*, vol. 78, pp. 1964–1966, 2001.
- [15] C. Gmachl, F. Capasso, D. L. Sivco, and A. Y. Cho, “Recent progress in quantum cascade lasers and applications,” *Rep. Prog. Phys.*, vol. 64, pp. 1533–1601, 2001.
- [16] T. Matsuoka, E. Kobayashi, K. Taniguchi, C. Hamaguchi, and S. Sasa, “Temperature dependence of electron mobility in InGaAs/InAlAs heterostructures,” *Jpn. J. Appl. Phys.*, vol. 29, pp. 2017–2025, 1990.
- [17] W. Walukiewicz, J. Lagowski, L. Jastrzebski, P. Rava, M. Lichtensteiger, C. H. Gatos, and H. C. Gatos, “Electron mobility and free-carrier absorption in InP; determination of the compensation ratio,” *J. Appl. Phys.*, vol. 51, pp. 2659–2668, 1980.
- [18] H. C. Liu and F. Capasso, *Intersubband Transitions in Quantum Wells, Physics and Device Application I, Semiconductor and Semimetals*. San Diego, CA: Academic, 2000, vol. 62, p. 11.
- [19] M. S. Vitiello, G. Scamarcio, V. Spagnolo, D. G. Revin, J. Cockburn, M. J. Steer, and R. J. Airey, “Electronic spatial distribution of $\text{In}_{0.53}\text{Ga}_{0.47}\text{As}/\text{AlAs}_{0.56}\text{Sb}_{0.44}$ quantum-cascade lasers,” *J. Appl. Phys.*, vol. 98, pp. 086106-1–086106-3, 2005.

Zhijun Liu received the B.S. and M.S. degrees in physics from Sichuan University, Chengdu, China, in 2000 and 2003, respectively. He is currently working toward the Ph.D. degree at the Department of Electrical Engineering, Princeton University, NJ.

His research focuses on high-performance quantum-cascade lasers.

Mr. Liu has won the 2007–2008 Wallace Memorial Fellowship at Princeton University.

Claire F. Gmachl received the Ph.D. degree (*sub auspiciis praesidentis*) in electrical engineering from the Technical University of Vienna, Austria, in 1995.

In 1996, she joined Bell Laboratories, Lucent Technologies, Murray Hill, NJ, as Postdoctoral Member of Technical Staff to work on quantum-cascade laser devices and microcavity lasers. In March 1998, she became a Member of Technical Staff in the Semiconductor Physics Research Department and a Distinguished Member of Staff in 2002. In September 2003, she joined Princeton University as an Associate Professor in the Department of Electrical Engineering and adjunct faculty to PRISM. She is the Director of MIRTHIE, the newly formed National Science Foundation (NSF) Engineering Research Center on Mid-Infrared Technologies for Health and the Environment. She has authored and co-authored more than 160 publications, has given more than 100 presentations at conferences and seminars, and holds 26 patents.

Dr. Gmachl is an Associate Editor for *Optics Express* and a member of the IEEE/LEOS Board of Governors. She is a 2005 MacArthur Fellow, has won various awards, and is a member of several professional societies.

Liwei Chen received the M.S. degree in electrical engineering from University of Maryland, Baltimore County, in 2006, where he is currently working toward the Ph.D. degree.

His research work focus on III–V compound MOCVD growth, process, and characterization of semiconductor lasers.

Fow-Sen Choa (M'88–SM'93) received the B.S. degree from National Taiwan University, Taipei, Taiwan, R.O.C., 1980 and the M.S. and Ph.D. degrees from the State University of New York, Buffalo, in 1988, all in electrical engineering.

After his Ph.D. work on femtosecond infrared lasers and detectors, he went to AT&T Bell Laboratories, Holmdel and Murray Hill, NJ and worked in the area of photonic integrated circuits and Crystal growth. He joined University of Maryland, Baltimore County, in 1991. He works in the areas of III–V compound semiconductor material growth and processing, optoelectronic devices for WDM switches and systems, RF-photonic devices, mid-IR and biophotonic devices. He has authored and co-authored more than 215 referred publications.

Prof. Choa is a Fellow of OSA and an Associate Editor of the *Journal of High Speed Networks*. He has been a Topical Editor of *Optics Letters* for six years.

Fred J. Towner received the B.S. degree in physics from the Pennsylvania State University, University Park, in 1986 and the M.S. degree in electrical engineering from the University of Maryland, Baltimore County, in 1992.

In 1986, he joined Martin Marietta Laboratories, Baltimore, MD, and worked in the areas of optoelectronics and crystal growth. In 1997, he joined Quantum Epitaxial Designs, Bethlehem, PA and worked with the large scale production of epiwafers. In 2002, he joined Maxion Technologies, Inc., College Park, MD, to head crystal growth efforts in support of the companies IR laser programs.

Xiaojun Wang received the Ph.D. degree in physics from XiaMen University, China, in 1994.

As part of his Ph.D. thesis and his postdoctoral research, he worked on the high-power 980- and 808-nm lasers in the Institute of Semiconductors, Chinese

Academy of Sciences, China, from 1992 to 1997. In Feb. 1998, he joined the Electrical Engineering Department, University of Maryland, Baltimore County, as Research Associate and then Research Scientist, working on InP-based optoelectronic components for optical fiber communication. In 2000, he joined Nortel Networks, MA, as a Senior Device Engineer, working on the 1310-nm single transverse mode pump lasers and MEMS based C-/L-band, widely tunable high-power external-cavity lasers. In 2003, he joined AdTech Optics, Inc., City of Industry, CA, as a Senior Engineer, mainly responsible for the product development of $\sim 13\text{-}/\sim 15\text{-nm}$ EML/DFB laser. Currently he serves as director of chip development, mainly focus on the quantum cascade lasers covering wavelength in the midinfrared range. He has authored and co-authored over 50 refereed publications.

Jenyu Fan received the Ph.D. degree in electrical engineering from University of Maryland Baltimore County, in 1999.

In August 1999, he joined Nanovation Technologies, Inc., at Evanston, IL, as a member of the research staff investigating a high-speed modulator. From 2000 to 2002, he worked for LightCross, Inc., Monterey Park, CA. He designed photonic integrated circuit based on AWG, VOA, power splitter, and waveguide components on silicon-on-insulator (SOI) material. Currently, he is with AdTech Optics, Inc., City of Industry, CA, where he works on InP-based laser and modules. He contributes in DFB, electro-absorption modulator integrated with DFB lasers (EML), FM laser, and FM-laser-based modulation for microwave-photonic links. He also contributes in mid-IR quantum cascade lasers. He has authored and co-authored more than 40 refereed publications and holds one U.S. patent.